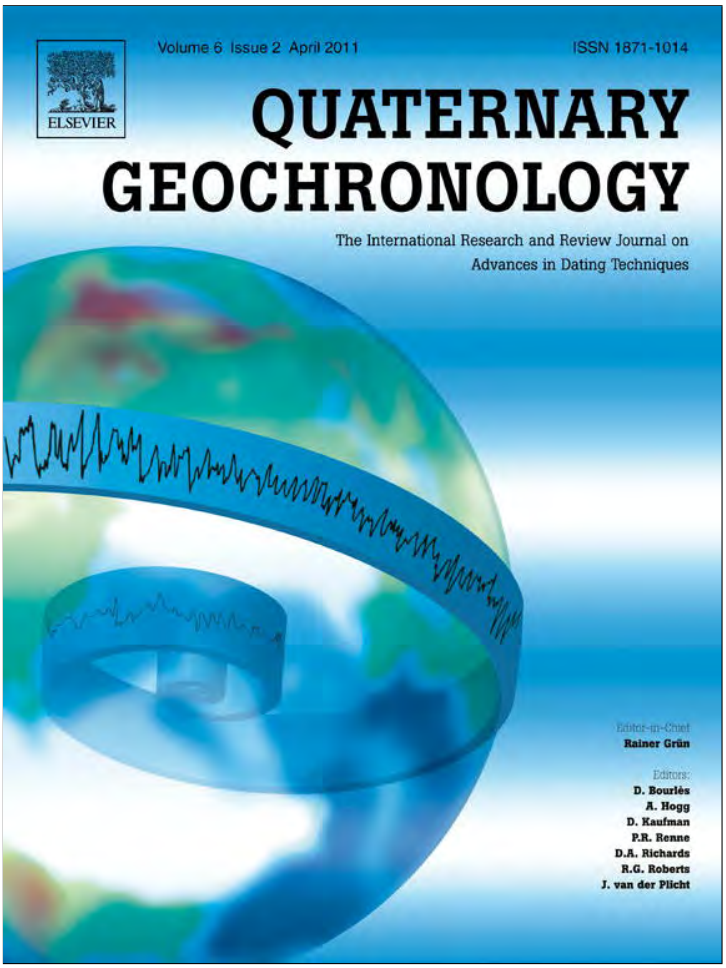

Quaternary Geochronology 6 (2011) 246–260

Contents lists available at ScienceDirect

Quaternary Geochronology

journal homepage: www.elsevier.com/locate/quageo

Research Paper

Erosion rates in an active orogen (NE-Taiwan): A confrontation of cosmogenic measurements with river suspended loads

L.L. Siame [a,f,g,*], J. Angelier [b,f,g], R.-F. Chen [c], V. Godard [a,f,g], F. Derrieux [a], D.L. Bourlès [a,f,g], R. Braucher [a,f,g], K.-J. Chang [d], H.-T. Chu [e,f,g], J.-C. Lee [c,f,g]

[a] CEREGE (Centre Européen de Recherche et d'Enseignement des Géosciences de l'Environnement), U.M.R 6635 CNRS-Aix-Marseille Université, B.P. 80, Plateau de l'Arbois, 13545 Aix-en-Provence cedex 4, France
[b] Géoazur, La Darse, B.P. 48, 06235 Villefranche-sur-Mer Cedex, France
[c] Institute of Earth Sciences, Academia Sinica, 128 Academia Road Sec. 2, Nankang, Taipei 115, Taiwan, ROC
[d] National Taipei University of Technology, Department of Civil Engineering, 1, Sec. 3, Chung-Hsiao E. Rd., Taipei 106, Taiwan, ROC
[e] Central Geological Survey, P.O. Box 968, Taipei, Taiwan, ROC
[f] LIA (Associated International Laboratory), France
[g] ADEPT (Active Deformation and Environment Programme for Taiwan), Taiwan

ARTICLE INFO

Article history:
Received 29 April 2010
Received in revised form
14 October 2010
Accepted 5 November 2010
Available online 12 November 2010

Keywords:
Denudation rates
Erosion rates
In situ-produced cosmogenic ^{10}Be
Taiwan

ABSTRACT

The direct and feedback relationships between tectonics, climate and denudation are a matter of debate. A better understanding of these relationships requires quantifying rates of denudation in a wide range of climate and tectonic settings, as well as at various time and space scales. Because of an ongoing active collision implying high uplift rates and a climate prone to extreme rainfall events and frequent tropical typhoons facilitating strong erosion dominated by mass movements and high degree of fluvial transport, the Taiwan environment is highly dynamic. In this work, spatially-averaged denudation rates determined along the network of one of the major rivers in Taiwan (Lanyang River) from in situ-produced cosmogenic nuclides (^{10}Be) measured in river-borne quartz minerals are compared to the erosion rates determined from the statistical analysis of modern sediment load data. Integrated over the last several hundreds of years, the denudation rate derived from in situ-produced ^{10}Be concentrations averages 2 ± 1 mm/yr within the Lanyang watershed. Integrated over the last 50 years, the erosion rate given by modern sediment load data is 5–7 mm/yr within the same catchment area. The studied catchment being characterized by a relatively low-level of human activity, the discrepancy between the two rates is most probably due different sensibilities to high-frequency, stochastic erosional events (typhoons and earthquakes). The cosmogenic-derived denudation rates can thus be regarded as more representatives for quantifying erosion processes on the short-time scale, and be strictly compared to the long-term exhumation rates derived from low-temperature chronological data.

1. Introduction

Earth's surface evolution and morphogenesis mainly result from the combined actions of internal (*i.e.*, volcanic activity and tectonics) and external (*i.e.*, weathering and erosion) processes. Tectonic processes set the initial conditions forcing surface uplift and, in regions of continuous tectonic activity, renewing topography as it is eroded. Climatic processes sculpt the Earth's surface through geomorphic processes acting on hillslopes or riverbeds for example. Numerous studies underlined the importance and the complexity of interactions and coupling relationships between tectonics, erosion and climatic processes (e.g., Beaumont et al., 2000; Willett, 1999; Whipple and Meade, 2004). However, the debate is still open and several coupling mechanisms very likely act together on the control of topographic evolution (Molnar and England, 1990; Molnar, 2003). Such actions and reactions have been modeled (Willett, 1999; Willett et al., 2001; Whipple et al., 1999; Koons, 1989; Beaumont et al., 1992; Montgomery and Brandon, 2002) but not often been documented in the field. Within this general context, quantifying pattern and magnitude of denudation processes on various time and space scales is essential, for example, to validate and calibrate the parameters to be supplied to landscape evolution models or to evaluate the isostatic response to erosional unloading in connection with tectonic modeling.

* Corresponding author. CEREGE (Centre Européen de Recherche et d'Enseignement des Géosciences de l'Environnement), U.M.R 6635 CNRS-Aix-Marseille Université, B.P. 80, Plateau de l'Arbois, 13545, Aix-en-Provence cedex 4, France. Tel.: +33 442971760.
E-mail address: siame@cerege.fr (L.L. Siame).

1871-1014/$ – see front matter © 2010 Elsevier B.V. All rights reserved.
doi:10.1016/j.quageo.2010.11.003

In this article, we investigate at the drainage basin scale the rates at which the topography of an active orogen is being eroded. To achieve this goal, we compare spatially-averaged denudation rates determined from cosmogenic nuclides (^{10}Be) measured in river-borne quartz minerals with the statistical analysis of modern sediment load data along the same river network. To apply this approach, we focused on the Taiwan Island (Fig. 1A), where the obliquity of the convergence between the Philippine Sea Plate and Eurasia involves the progressive subduction of the continental margin of China, and induces the fast growth of the Taiwan Mountains. Indeed, because of the high rate of plate convergence (~9 cm/yr), deformation and erosion rates are extreme. Today, the orogen culminates at about 4000 m, and rose from the sea level only a few million years ago. Within such a context, the impacts of climate and surface processes are particularly well-expressed, allowing studying their interaction with tectonic processes. Taiwan is thus a natural laboratory, where a complete sequence of mountain building processes can be studied from oceanic subduction (South Taiwan) to mature continental subduction (Central Taiwan), and orogenic wedge collapse in a back-arc context (North Taiwan).

In this paper, we focused on the Lanyang River watershed, which drains the Backbone and the Hsüehshan mountains in Northeastern Taiwan (Fig. 1B). Since it is located in the part of the orogenic wedge where collapse is ongoing, this area might be characterized by relatively low erosion rates compared to the central part of the mountain belt. Indeed, using suspended sediment observations smoothed at catchment scale, Dadson et al. (2003) have shown that northern Taiwan is experiencing modern rates lower than 10 mm/yr whereas they can reach values higher than 15 mm/yr in the eastern Central Range.

The Lanyang watershed has thus been selected as a test site for the quantification of the denudation rates using measurements of cosmogenic ^{10}Be in river-borne sediments in such a dynamic environment. Moreover, the Lanyang River is also well-instrumented with hydrological stations allowing the comparison of ^{10}Be-derived erosion rates with the analysis of river suspended loads.

Hereafter, we first present a review of the published erosion and denudation rates in Taiwan. We then consider the geomorphic context of the Lanyang River, where we explore the denudation rates based on in situ-produced cosmogenic ^{10}Be in river-borne quartz minerals, and modern erosion rates derived from suspended load data. Finally, we discuss the results independently obtained through these different approaches, trying to highlight the most critical observations for unraveling the erosional conditions that prevail in this area of the Taiwan mountain belt.

2. Review of published erosion rates in Taiwan

The present-day erosional context of the Taiwan Island is controlled by high uplift rates and a strong sub-tropical climate. On average, three typhoons hit the island during the wet season (May to October). These typhoons commonly follow preferential westward pathways, which are mainly controlled by air currents and relief distribution. In Taiwan, most of the erosion is achieved by runoff on hillslopes and transport by rivers with a predominance of suspended and bed loads (Lee, 1976; Li et al., 2005). Moreover, the erosional role of landslides that break away the rock masses and promote rapid outgoing sedimentary fluxes by rivers is particularly important (Hovius et al., 2000; Chen et al., 2005). In turn, the high rates of erosion affecting the island of Taiwan are thought to have a major positive feedback on the tectonic processes by involving high exhumation and uplift rates to compensate for the loss of mass. This feedback is believed to produce a balance between the processes of tectonic accretion and outgoing eroding flows, leading to steady-state topography (Fuller et al., 2006).

For the last thirty years, the erosion rates have been studied in Taiwan by methodological approaches spanning two very different time scales: the short-term (a few decades) from the analysis of the river suspended loads, and the long-term (several hundred of thousands to a few millions of years), using data from low-temperature thermo-chronology and associated thermo-mechanical models. The pioneering study by Lee (1976) involved a calibration

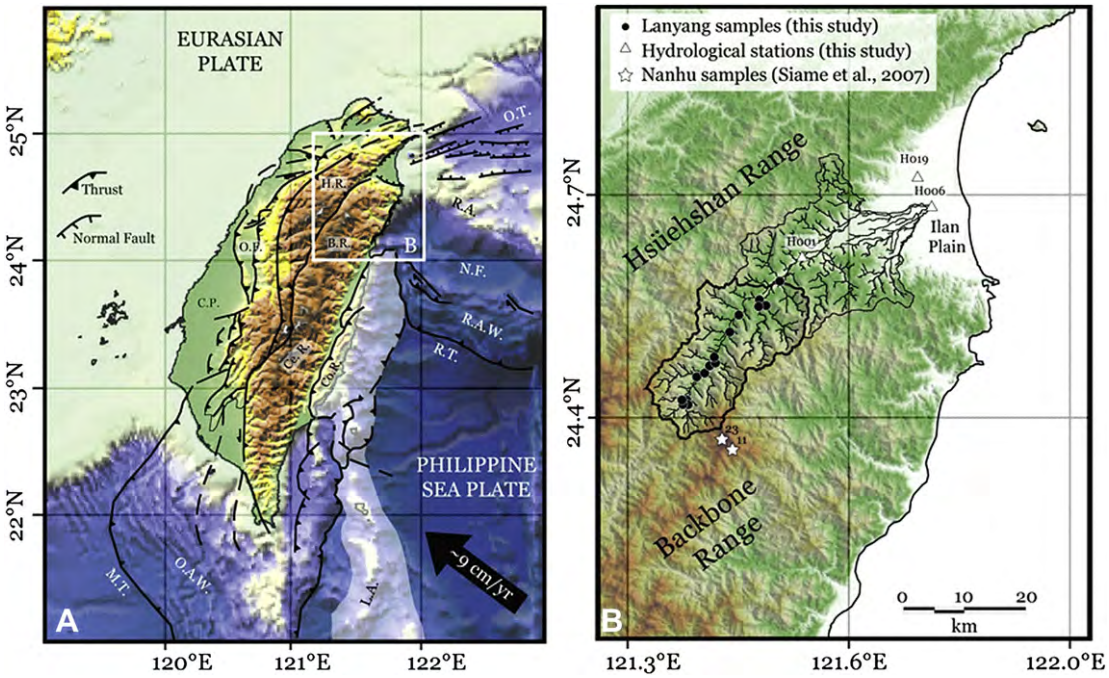

Fig. 1. A: General geodynamic map of Taiwan. Keys: M.T., Manilla Trench; O.A.W., Oceanic Accretionary Wedge; L.A., Luzon Arc; R.T., Ryukyu Trench; R.A.W., Ryukyu Accretionary Wedge; N.F., Nanao Forearc; R.A., Ryukyu Arc; O.T., Okinawa Trench, Co.R., Coastal Range; Ce.R., Central Range; B.R., Backbone Range; H.R., Hsüehshan Range; I.F., Inner Foothills; O.F., Outer Foothills; C.P., Coastal Plain. B: Map of North-eastern Taiwan localizing the studied Lanyang River watershed, the sampled sites for cosmogenic ^{10}Be measurements and hydrological stations used in this article.

method linking water discharge and river suspended load, which led this author to propose an average erosion rate of 5.5 mm yr^{-1} in the Central Range. Fuller et al. (2003) have coupled such a deterministic approach with a stochastic modeling of the hydrological signal temporal variations, and estimated erosion rates ranging between 2.2 and 8.3 mm yr^{-1} in the Eastern Central Range. Dadson et al. (2003) used the suspended loads of more than one hundred hydrological stations spread across Taiwan, as well as an estimation of the bed load component to propose a mean erosion rate of 5.2 mm yr^{-1} for the whole range of Taiwan, and of approximately 6 mm yr^{-1} for the Central Range. More recently, revaluations of hydrological data for some rivers (Li et al., 2005) have yielded suspended load values systematically lower than those reported in the previous studies (e.g., Lee, 1976; Dadson et al., 2003), underlining that the bias in data collection could lead to an overestimation of the suspended load and that large datasets are required in order to reduce uncertainty and mitigate the effects of temporal variations.

Dadson et al. (2003) have also used fission track data combined with a one-dimensional thermo-mechanical model to propose a long-term rate of erosion ranging between 1 and 10 mm yr^{-1} for the whole range, and 3–6 mm yr^{-1} for the Central Range. Willett et al. (2003) took a similar approach for the Eastern Central Range where they determined long-term rates of erosion in the range of 4–6 mm yr^{-1}. The results of these recent studies are in close agreement with those of precursor ones by Liu (1982), Liu et al. (2000, 2001) which have determined a long-term rate of erosion ranging between 2.5 and 4.6 mm yr^{-1} in the Central Range. More recently, Fuller et al. (2006) and Simoes et al. (2007) have integrated new low-temperature thermo-chronology data and those of the literature to feed two-dimensional thermo-mechanical and thermo-kinematic models including heat flux calibrations. Those studies allowed a reassessment of the long-term rates of erosion throughout the Taiwan belt to be ranging between 2.3 mm yr^{-1} (Fuller et al., 2006) and 3.2 mm yr^{-1} (Simoes et al., 2007).

The comparison between the results issued from these studies suggests that the rates determined from the low-temperature thermo-chronology data and associated models are substantially lower than those determined from the modern hydrological records. This apparent discrepancy between long-term and short-term rates is most probably due to the differences in characteristic time scales underlying both methodological approaches. Due to the high importance of stochastic erosional events (e.g., Dadson et al., 2003), the question is whether or not the erosion rates determined from modern hydrological records are representative for long-term geological processes. This issue is particularly important in highly dynamic environments such as Taiwan. To be able to compare rates of erosion integrated over short and long-term periods of time, it is thus necessary to apply another approach that bridges the gap between those two time scales and is less sensitive to high-frequency erosional events. The method based on in situ-produced cosmogenic ^{10}Be in river-borne quartz minerals responds to this requirement, and allows opening the short-term time window (see Section 4).

3. The Lanyang watershed

3.1. Geological setting

The Ilan Plain is a deltaic plain characterized by a flat topography close to the sea level, and surrounded by the high mountains of the Hsüehshan Range to the northwest, and those of the Backbone Range to the Southeast (Fig. 1B). In this area of the Taiwan belt, the orogen suffers an overall collapsing, which is driven by the westward, onshore propagation of the Okinawa back-arc trough.

The Ilan Plain is essentially fed by the Lanyang River, the second largest river in northern Taiwan (Fig. 1B). The Lanyang River discharges annually roughly 10 million tons of sediment (Liu et al., 2006) into the southwestern submarine head of the Okinawa Trough. This river takes its source at an elevation of 3536 m in the vicinity of the Nanhutashan and Hsüehshan summits (Fig. 2). Along most of its course, the Lanyang River follows the trend of the Lishan Fault (Fig. 2A) that separates two major geological provinces: the Hsüehshan Range to the west and the Backbone Range to the east (Ho, 1986; Lee et al., 1997).

On the western side of the Lanyang Valley (Fig. 2), the Hsüehshan Range consists of Paleogene continental margin sediments, mostly Eocene and Oligocene in age, from the Kankou, Chiayang, and Peileng formations. The Kankou Formation (OS) is mainly composed of hardened argillite or phyllitic slate, with rare sandy interbeds. The Chiayang Formation (EO1) is mainly composed of a thick series of slate with minor fine-grained sandstone and siltstone intercalations. The Peileng Formation (EO2) is composed of the Szeleng Sandstone, which is replaced by the Meichi Sandstone in the eastern part of the Hsüehshan Range belt. The Szeleng Sandstone is characterized by thick-bedded, quartzitic sandstone intercalated with dark gray argillite or slate. The Meichi Sandstone is mainly composed of well-bedded, fine- to coarse-grained compact sandstone and alternating sandstone and dark argillite. On the eastern side of the Lanyang Valley (Fig. 2), the Backbone Range is characterized by the Miocene Lushan Formation (Ml), which consists mostly of black to dark gray argillite, slate, and phyllite with local interbeds of fine-grained metamorphosed sandstone and quartz veins.

To evaluate the surface hardness of the rocks that are eroded in the Lanyang Watershed, we used a Schmidt impact hammer, as described in the review paper by Aydin and Basu (2005). When the piston of the hammer is released, the impact energy is largely dispersed by plastic deformation and transformation into heat and sound, the remaining energy being a proxy for the impact penetration resistance of the rock surface. The harder the rock surface, the greater is the rebound value. Repeated experiments provide a reliable index of rock surface hardness (Aydin and Basu, 2005). At each site, a series of ten measurements were made by pressing the Schmidt hammer orthogonally against the surface of the bedrock, resulting in a mean rebound value and standard deviation. The data are reported in Annex 1 and summarized in the graph of Fig. 2C. 46 measured sites were distributed over the Lanyang watershed and focused on the prominent geological formations (Fig. 2). Thus, on the Hsüehshan Range side, 10 sites belong to the Kankou Formation (OS) and 10 other sites belong to the Peileng Formation (EO2). On the Backbone Range side, 26 sites were measured in the Lushan Formation (Ml). To illustrate the statistical distribution of the Schmidt hammer measurements, we plotted the Gaussian probability distributions (see Annex 1) of the rebound values for the three main geological formations as well as for the main lithologies (Fig. 2). Those curves illustrate the fact that the surface hardness for the prominent lithologies are on the same order of magnitude, independently of the stratigraphic age of the formations. In other words, the slates and sandstones of the Eocene-Oligocene formations located on the left-hand side of the Lanyang Valley are characterized by surface hardness values that do not significantly differ from those obtained in the Miocene formation on the right-hand side of the Lanyang Valley (Fig. 2). The only lithological difference one can underline is that the Lushan formation is richer in slates than the Eocene-Oligocene formations located on the left-hand side of the Lanyang Valley. This difference in sandstone-slate proportions acts as a first order lithological control, resulting in a left-hand side with steeper slopes and shorter drainage basins than the right-hand side of the Lanyang Valley (Fig. 2).

3.2. Geomorphic setting of the Lanyang Valley

To investigate the geomorphic characteristics of the Lanyang watershed, the stream segments and basin boundaries have been

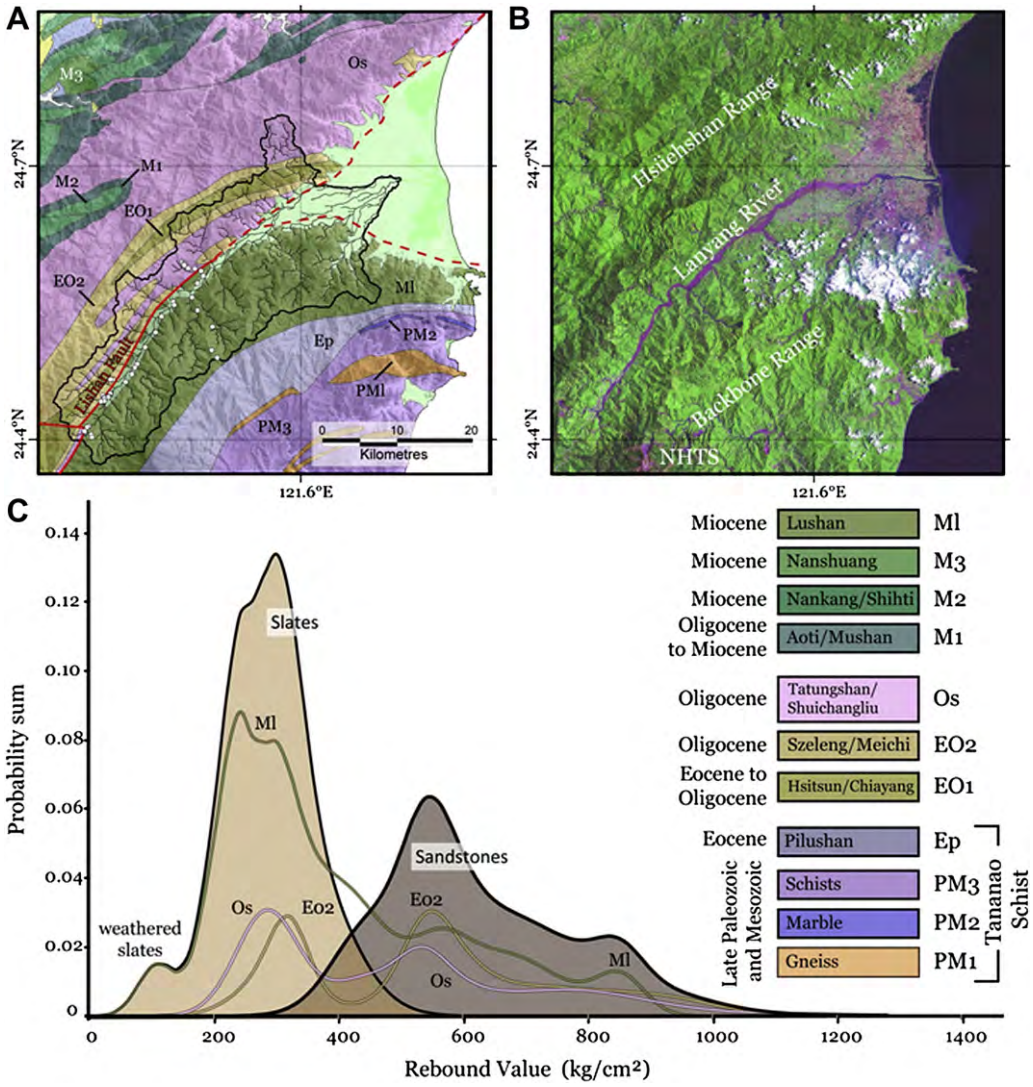

Fig. 2. A: Geological map centered on the Lanyang River and Ilan Plain area (Geological units from the 1/500,000 geological map of Chen et al., 2000). The solid black line delineates the Lanyang watershed extracted from the 40-m resolution digital topographic database. The white dots refer to sites of in situ Schmidt hammer measurements (Annex 1). B: Landsat (Enhanced Thematic Mapper, ETM+) image extract centered on the Lanyang River and Ilan Plain area (NHTS: Nanhutashan). C. Cumulative probability curves for the in situ Schmidt Hammer measurements of rebound values (Annex 1).

extracted from a digital elevation model (with a resolution of 40 m per pixel) using the Rivertools™ software. The organization of the channels was done according to the method of Strahler (1957). In order to restrict our basin analysis to the relevant area for this study, the extracted Lanyang watershed corresponds to the catchment located upstream of the gauging station number H006 in the Ilan Plain, the closest gauging station to the sea shore (Fig. 1B).

Upstream of this gauging station H006, the Lanyang watershed is of 7th stream order, with 4 sub-basins of 6th stream order (Table 1). The 7th stream order watershed is characterized by a basin area of 821 km^2, and a main river length of 76 km (Table 1). When grouped by stream order, the averaged planimetric geomorphic properties grow or decrease following geometric progressions (Fig. 3A–E) that are linked to the self-similar nature of river networks (Horton, 1932, 1945). The topological indices of the Lanyang River network, such as bifurcation ratios, drainage and source densities (Table 1), converge towards values suggesting that this river is characterized by a low flooding potential.

When grouped by stream orders, the averaged relief values grow following a geometric progression from an average value of 0.09 km for basins of 1st Strahler order to a maximum value of 3.4 km for the 7th stream order watershed (Fig. 3F). In the Lanyang watershed, two groups of hypsometric integral values can be depicted (Fig. 3G). The sub-basins with Strahler orders ranging from 1 to 3 are characterized by higher hypsometric integral values on the order of 0.5 whereas the sub-basins with Strahler orders ranging from 4 to 7 are characterized by lower hypsometric integral values on the order of 0.2 (Table 1). Together with the source density values (Table 1), this most probably reflects the fact that the sub-basins of stream order lower than 4 have a greater capacity to generate new streams than those of higher stream orders. This is probably due to the fact that sub-basins of Strahler orders higher than 4 are geomorphically more mature than sub-basins of lower Strahler orders.

3.3. Shear stress along the Lanyang Valley

We consider that the geomorphic and tectonic context of Taiwan allows us to use fluvial shear stress as a reliable proxy for the intensity of fluvial processes associated with erosion. We also make the assumption that fluvial incision is the primarily driving factor for erosion at the landscape scale, as it regulates the intensity of hillslope processes (e.g., Burbank, 2002; Simpson and Schlunegger, 2003).

Table 1
Geomorphic properties of the Lanyang River extracted from the 40 m-resolution grid.

Order	1	2	3	4	5	6	7
Number of basins	5697	1258	277	66	14	4	1
Basin Area (km^2)	0.1	0.4	1.7	8.2	38.7	142.6	820.7
Diameter (km)	0.5	1.0	2.2	4.9	10.9	19.2	56.3
Shape factor	0.6	0.6	0.6	0.6	0.6	0.6	0.5
Basin Relief (km)	0.1	0.3	0.6	1.0	1.6	2.1	3.4
Hypsometric Integral value	0.5	0.5	0.4	0.2	0.2	0.2	0.3
Total Channel Length (km)	0.3	1.3	5.9	28.3	132.5	490.3	2838.1
Longuest channel length (km)	0.3	0.9	2.3	6.1	15.7	27.0	76.1
Along-channel Length (km)	0.3	0.5	1.2	3.2	8.4	6.6	39.9
Along-channel Slope	0.4	0.3	0.2	0.1	0.0	0.0	0.0
Drainage density (km/km^2)	3.3	3.7	3.6	3.5	3.4	3.5	3.5
Source density (km/km^2)	19.1	10.2	7.8	7.3	7.2	7.1	7.0
Bifurcation ratios	2nd–1st	3rd–2nd	4th–3rd	5th–4th	6th–5th	7th–6th	
	4.5	4.5	4.2	4.7	3.5	4.0	

The bifurcation ratio derives from the "law of stream number" defined by Horton (1945). This parameter reveals the possibility for a given watershed to localize or not flooding events. This parameter is calculated as the ratio of the number of streams of any order to the number of streams of the next highest order. Theoretically, values of bifurcation ratio cannot be lower than 2, and natural values of bifurcation ratio are generally comprised between 3 and 5 where the lithology is relatively homogeneous (Summerfield, 1991; Peckham, 1995). Low values of bifurcation ratio indicate a higher probability of flooding because the running water tends to concentrate in one channel rather than to spread out over the watershed (e.g., Strahler, 1964). The drainage density (Strahler, 1958) reflects a balance between erosion and ground surface resistance (Summerfield, 1991). This parameter is expressed as the ratio between the cumulative length of all streams and the basin area. Related to climate and lithology (Ritter et al., 1995), this parameter provides a valuable tool to assess landscape dissection and runoff potential. Drainage densities show a wide range of values, from less than several km^{-1} on permeable sandstone to several hundreds of km^{-1} on unvegetated badlands (Craig et al., 1988; Summerfield, 1991). Generally speaking, high values of drainage density typically indicate a rapid rainfall response, that is to say a high flooding potential. The source density is generally considered as an indicator of the capacity of a given watershed to generate new streams. This parameter is calculated from the ratio of the number of sources in a river network to the area of the corresponding drainage basin. The hypsometric integral value, related to the degree of dissection of a given landscape, is commonly used to discriminate between tectonically active and inactive regions (Strahler, 1952). Values of the hypsometric integral close to 1 indicate youthful or rejuvenated topographies whereas intermediate to low values are related to more matured and dissected landscapes.

The key geomorphic parameters necessary for the shear stress calculation are extracted from the 40 m-resolution DEM or derived through simple scaling relationships.

Basal shear stress due to flowing water on the river bottom can be computed as:

$$\tau = \rho g R S \tag{1}$$

where ρ is the water density, g the gravity acceleration, R the hydraulic radius and S the channel slope. For large streams R can be approximated by H, the flow depth, and the average velocity of the flow can be obtained by mass conservation and Manning's equation (Lavé and Avouac, 2001):

$$U = \frac{Q}{W.H} = \frac{1}{N} H^{2/3} S^{1/2}. \tag{2}$$

According to this relation, the basal shear stress can be expressed as

$$\tau = \rho g \left(\frac{Q.N}{W}\right)^{3/5} S^{7/10}. \tag{3}$$

Since strong seasonal contrasts exist in Taiwan (Hartshorn et al., 2002), we consider peak-flow conditions in our computation, as they are responsible for most of the effective morphogenetic processes (Tucker and Bras, 2000). We used the same dataset as for Section 5 to derive a scaling relationship between contributing area A and the 10 years return discharge Q_{10}, which can be expressed as:

$$Q_{10} = 0.03 A^{1.1}. \tag{4}$$

Considering that discharge is almost linearly related to contributing area, we used the classical relation $W \propto Q^{1/2}$to scale channel width with area. At last, as we do not have constraining data to evaluate changes in bed load size across the Lanyang watershed, we consider that roughness N is constant over our study area.

Along the river network, the computed shear stress values are interpolated to produce a continuous shear stress map for the Lanyang watershed (Fig. 4). The main control on the value of shear stress is channel slope. Localized patches of high shear stress can be observed and correlates with high gradients stream segments and knickpoints. For each basin where we obtained a cosmogenic-derived denudation rate (see Section 4), an average shear stress value was computed from the continuous shear stress map (Table 2). As they display significantly different sizes, basins corresponding to the main trunk and to the tributaries have been distinguished. This scale contrast may imply some important differences for the processes operating inside those catchments, and it may particularly affect the interpretation of the spatially-averaged parameters we are using here, such as basin-wide denudation rates and averaged shear stress. However, taking into account the uncertainties associated with the computed shear stress values, it seems that all the sub-basins in the studied part of the Lanyang Watershed display similar values of shear stress that are on the order of 51 ± 4 MPa (Table 2), implying that local shear stress variations with a length-scale of a few kilometers are filtered independently of the size of the watersheds.

4. Cosmogenic nuclide-derived denudation rates of the Lanyang river basin

4.1. The method

In situ-produced cosmogenic ^{10}Be concentrations measured in river-borne sands can be used to document hillslope exposure history and estimate basin averaged denudation rates (Bierman and Nichols, 2004; von Blanckenburg, 2005). Within the first meters of rock or soil below the earth's surface, the cosmogenic nuclide build-up in minerals is balanced by the radioactive decay of the nuclide and by the erosional and chemical processes acting on that surface (Lal, 1991). If exposure to cosmic rays is sufficiently long with respect to the denudation rates, the accumulation of in situ-produced ^{10}Be reaches a secular equilibrium concentration, allowing calculation of a maximum denudation rate (Lal, 1991). For specific geomorphic settings, such maximum denudation rates can

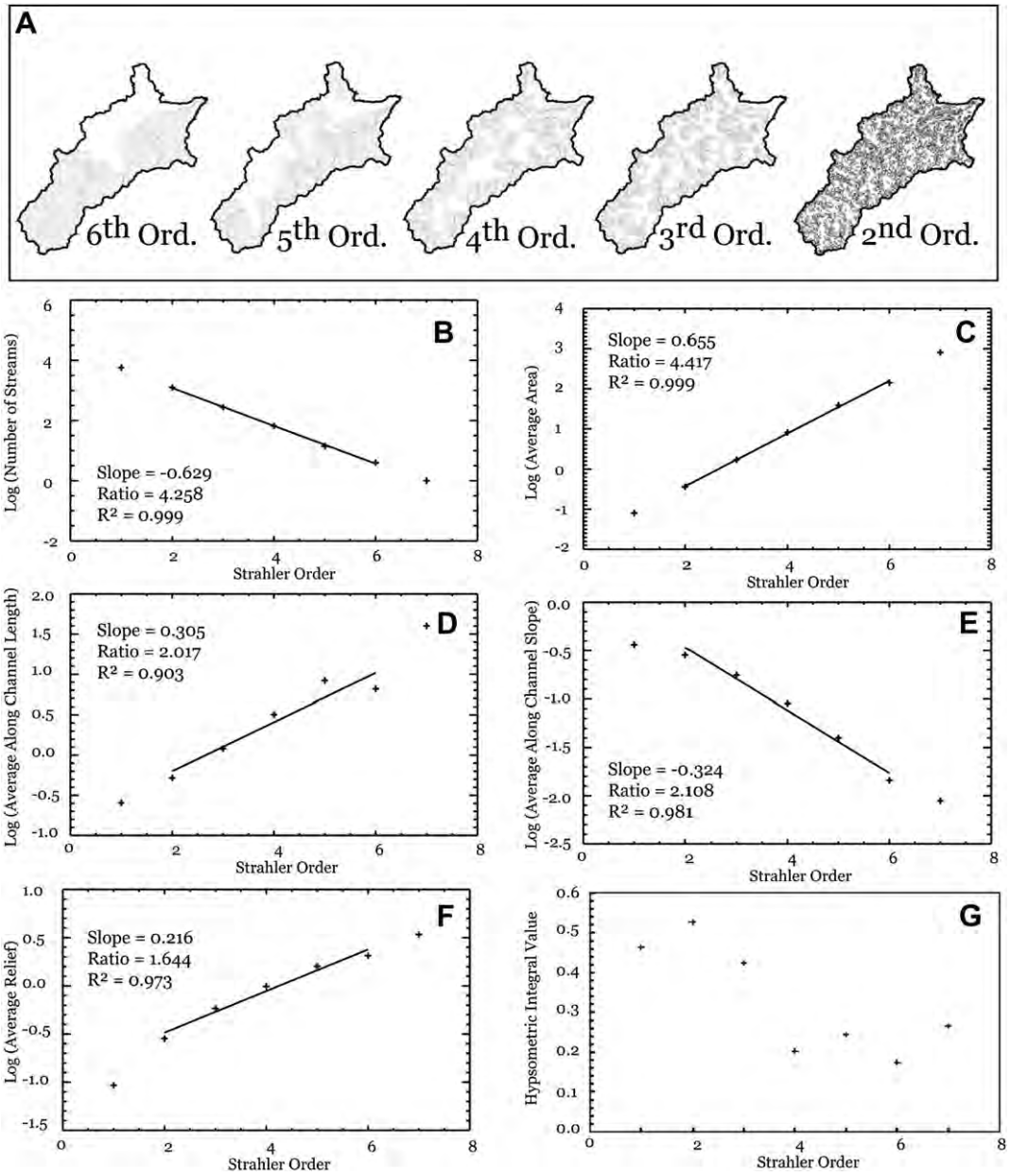

Fig. 3. A: Distribution pattern of the sub-basins extracted from the 40-m resolution digital topographic database for Strahler's stream order 2 to 6. B–G: Relationships between stream order and Lanyang watershed properties. For each correlation, the slope of the regression line, the stream ratio (factor by which the geomorphic property grow or decrease), and the square of the regression coefficient is indicated. For each regression, the first and last orders are not taken into account since (1) first order streams are at the transition between hillslope and channel, and (2) last order represent an averaged value for a single Strahler basin. Stream ratio values are presented in Table 1.

be measured along altitudinal transects (e.g., Riebe et al., 2004) or on mountain summits (e.g., Small et al., 1997; Siame et al., 2007). However, this approach only permits determining local bedrock denudation rates whose larger-scale significance may be questionable, and one may need numerous samples to reliably document magnitude and patterns of variation over an entire region. To spatially integrate cosmogenic-derived denudation rate, another approach consists in using the natural mixing of sediments issued from slope and fluvial processes within a given drainage basin (Brown et al., 1995, 1998; Granger et al., 1996).

Since the rivers carry and mix the sediment derived from the outcrops, soil-mantled hillslopes, and incised bedrock channels within the headwater areas, the drainage system is a natural spatial integrator of the denudation processes. On the hillslopes of the watershed, a given volume of rock is progressively brought to the surface through time by the denudation processes, and then progressively exposed to the secondary cosmic ray particles that are responsible for cosmogenic production (Lal, 1991; Gosse and Phillips, 2001). In other words, the cosmogenic build-up records the denudation history while the material is transferred upward through the upper meters of rock or soil, and thus integrates both the effects of physical (erosion) and chemical (weathering) processes acting at the earth's surface. Measurements of ^{10}Be concentrations in river-borne quartz minerals can be used to estimate rates of denudation at the basin scale, cosmogenic concentrations being simply proportional to the long term, basin-wide integrated denudation rate (Lal, 1991; Granger et al., 1996). This methodology have been tested for small (1–10 km^2; Granger et al., 1996) or large (10^2–10^5 km^2; Schaller

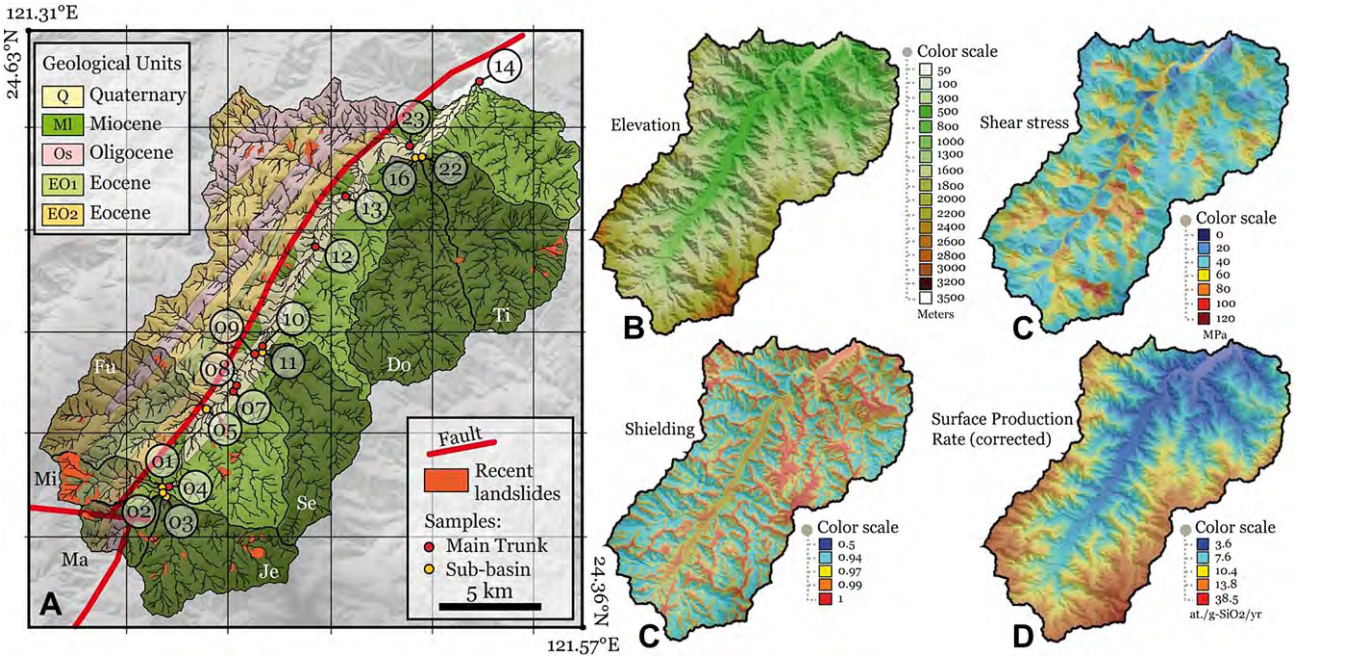

Fig. 4. A: Geological map of the upstream part of the Lanyang River localizing the sampling sites listed in Table 3. B: Elevation grid for the upstream part of the Lanyang River based on a 40-m resolution digital topography database. C: Shear stress grid calculated from the 40-m resolution digital topography database. D: Geomorphic shielding grid calculated from the 40-m resolution digital topography database using Dunne et al. (1999). D: *In situ*-produced ^{10}Be surface production rate grid calculated from the 40-m resolution digital topography database using Stone (2000) and a sea level, high latitude production rate of 4.5 atoms g^{-1} yr^{-1} (see text).

et al., 2001) drainage basins, as well as in different orogenic (Kirchner et al., 2001; Vance et al., 2003; Matmon et al., 2003) and climatic (Brown et al., 1998; Clapp et al., 2001; Schaller et al., 2001; von Blanckenburg et al., 2004) settings.

We used in situ-produced ^{10}Be resulting from spallation and muonic reactions on Silicon and Oxygen in quartz minerals. During sampling, a minimum of 1 kg of sediment were collected from sand deposits in the active stream beds. To assess the existence of any spatial variation of the cosmogenic-derived denudation rates, we sampled along the main trunk of the Lanyang River as well as at the outlets of several sub-basins contributing to the total denudation in the whole watershed (Figs. 4 and 5). After sieving (fraction comprised between 1 and 0.250 mm), sediment samples passed through magnetic separation, and non-magnetic fraction undergone selective etchings in fluorosilicic and hydrochloric acids to eliminate all mineral phases but quartz. Quartz minerals then undergone a series of selective etching in hydrofluoric acid to eliminate potential surface contamination by ^{10}Be produced in the atmosphere. The cleaned quartz minerals were then completely dissolved in hydrofluoric acid after addition in each sample of ~100 μl of an in-house 3×10^{-3} g/g ^{9}Be carrier solution prepared from deep-mined phenakite (Merchel et al., 2008). Hydrofluoric and Perchloric fuming was used to remove fluorides and both cation and anion exchange chromatography were used to eliminate iron, aluminium, manganese and other elements. Beryllium oxide was mixed to 325 mesh niobium powder prior to measurements by Accelerator Mass Spectrometry (AMS). Measurements were performed both at the old (TANDETRON, Gif-sur-Yvette, France) and

Table 2
Geomorphic properties of the drainage basins sampled for cosmogenic nuclide measurements.

Sample	Geology	River name	Localisation	Landslides % of basin area	Strahler order	Basin area (km^2)	Basin diameter (km)	Total length km	Mean slope (degrees)	Elevation (m)			Shear stress (MPa)	
										Mean	Min.	Max.	Value	error
Ilan-1	Olig.	Mimoden	LH-SB	18.8	4	8.6	5.6	27	36	1939	1152	2892	51.5	10.3
Ilan-2	Olig.	Madan	LH-SB	3.1	4	9.1	4.6	30	32	1763	1138	2583	42.5	9.3
Ilan-3	Mioc.	Jekejo	RH-SB		5	27.6	8.1	88	33	2151	1150	3512	58.8	18.2
Ilan-4	Both	Lanyang	MT	6.1	5	47.0	13.1	151	33	2007	1112	3512	53.2	17.1
Ilan-5	Olig.	Fubuer	LH-SB	1.1	5	25.8	8.4	78	35	1941	891	3130	58.7	14.1
Ilan-7a	Both	Lanyang	MT		6	110.7	14.6	348	32	1818	803	3512	52.4	18.2
Ilan-8	Both	Lanyang	MT		6	110.8	14.6	348	32	1817	794	3512	52.6	17.6
Ilan-9a	Both	Lanyang	MT		6	117.8	14.6	372	32	1776	719	3512	52.5	18.0
Ilan-10	Both	Lanyang	MT		6	160.1	16.4	491	32	1771	704	3512	52.7	18.6
Ilan-11b	Mioc.	Sechong	RH-SB		5	29.6	10.0	80	32	1839	731	3080	58.4	18.3
Ilan-12	Both	Lanyang	MT		6	200.5	20.3	617	31	1659	545	3512	52.1	18.4
Ilan-13	Both	Lanyang	MT		6	220.2	22.8	681	31	1613	474	3512	51.7	18.2
Ilan-14	Both	Lanyang	MT	1.7	7	376.4	31.6	1203	30	1408	279	3512	49.0	18.0
Ilan-16	Mioc.	Dowan	RH-SB		5	44.0	11.4	137	28	1352	370	2302	48.8	13.2
Ilan-22	Mioc.	Tiengouer	RH-SB	1.9	5	36.0	9.7	121	30	1171	377	2337	47.0	11.2
Ilan-23	Both	Lanyang	MT		6	263.5	27.8	829	31	1529	365	3512	51.0	18.3

Keys: Olig., Oligocene; Mioc., Miocene; LH-SB, Left-hand side sub-basin; RH-SB, Right-hand side sub-basin; MT, Main trunk.

Fig. 5. Photograph views of selected sampling sites along the Lanyang River Valley. A. Southward view of the headwater watersheds (1, Mimodenchi; 2, Madanchi; 3, Jekejochi). B. Photograph taken at the outlet of the Madanchi showing sample Ilan-2. C., Panoramic view of the Lanyang Valley at sampling site Ilan-13. D. View of the sampling site Ilan-7. E. View of the sampling site Ilan-14.

new (ASTER, Aix-en-Provence) AMS French facilities (Table 3). Together with the natural samples, blank samples were processed throughout the chemical steps, yielding isotopic ratios on the order of $(3.0 \pm 1.5) \times 10^{-15}$ which are within the range values resulting from long-term AMS measurements of chemically processed blank ratios (Raisbeck et al., 1987, 1994; Arnold et al., 2010) (Table 3). All ^{10}Be concentrations are normalized to ^{10}Be/^{9}Be SRM 4325 NIST reference material with an assigned value of $(2.79 \pm 0.03) \times 10^{-11}$. This standardization is equivalent to 07KNSTD within rounding error. The ^{10}Be half-life of $(1.39 \pm 0.01) \times 10^{6}$ years used is that recently recommended by Korschinek et al. (2009) and Chmeleff et al. (2009) according to their two independent measurements.

To determine basin averaged production rates, scaling factors for latitude and altitude corrections were calculated according to Stone (2000), for each cell of the 40 m-resolution digital topography database using the Cronus-Earth Matlab scripts (http://hess.ess.washington.edu/math/). Geomorphic shielding factors were calculated for each cell of the 40-m resolution digital topography database using a 10° azimuth step following Dunne et al. (1999). The resulting grids are shown in Fig. 4. For each sampled watersheds, we calculated basin averaged production rates using a modern ^{10}Be production rate at sea level and high latitude of 4.5 ± 0.3 atoms/g-SiO_2/yr to account for the reevaluation of absolute calibration of ^{10}Be AMS standards proposed by Nishiizumi et al. (2007), and took the unweighted mean values (Table 3).

To determine the denudation rates (ε) from the measured concentrations (N), we used the following equation:

$$N(x,t) = \frac{\overline{P}_n}{\frac{\varepsilon\cdot\rho}{\Lambda_n}+\lambda} + \frac{\overline{P}_{\mu s}}{\frac{\varepsilon\cdot\rho}{\Lambda_{\mu s}}+\lambda} + \frac{\overline{P}_{\mu f}}{\frac{\varepsilon\cdot\rho}{\Lambda_{\mu f}}+\lambda} \quad (5)$$

where $\overline{P}_n$ is the basin averaged spallation production rate, scaled for altitudinal and latitudinal variability (e.g., Stone, 2000), whereas $\overline{P}_{\mu s}$ and $\overline{P}_{\mu f}$ the basin averaged negative and fast muon production rates, scaled for altitudinal variability. Neutrons are very interactive particles and thus not very penetrative compared to negative and fast muons. To account for the density variability through the column of soil and rock exposed to cosmic rays on the hillslopes of the watersheds, we allowed this parameter to vary between 1.8 g cm^3 (soil) to 2.4 g cm^3 (rock). To account for the respective attenuation lengths of spallation and muonic particles at depth, we respectively used the value of $\Lambda_n = 160$ g/cm^2 for the neutrons (Gosse and Phillips, 2001), and the values of $\Lambda_{\mu s} = 1500$ g/cm^2 (negative muons) and $\Lambda_{\mu f} = 5300$ g/cm^2 (fast muons), based on natural samples from a sub-vertical Brazilian lateritic quartz vein (Braucher et al., 2003).

4.2. Reliability of the cosmogenic-derived denudation rates

To assess whether the denudation rates derived from the measured in situ-produced ^{10}Be concentrations are reliable or not, the ^{10}Be/^{9}Be isotopic ratios measured within the samples have been compared to those of the companion blank processes using the statistical chi-square approach described by Ward and Wilson (1978). Taking into account the associated uncertainties, this approach allows determining if two samples are significantly different from one another. This comparison is crucial since the measured isotopic ratios are particularly low (on the order of 10^{-15}). The chi-square threshold at 95% confidence for one degree of freedom (2 samples) is 3.8 (Table 3). If the chi-square test value is higher than the chi-square threshold, then the isotopic ratio measured in the sample is significantly different from that of the blank process. In that case, a reliable in situ-produced ^{10}Be concentration can be calculated and a reliable denudation rate can be derived from equation (5) (Table 3). If the chi-square test value is lower than the chi-square threshold, then the isotopic ratio measured in the sample is not significantly different from that of the blank process. In that case, only maximum bounding values can be proposed for the ^{10}Be concentration, yielding a minimum value for the denudation rate, using Granger et al. (1996) formulation (Table 3). From our group of sixteen samples only eight have passed that statistical test. However, this strengthens the confidence we have in the geological significance of the denudation rates derived from those eight samples.

4.3. Cosmogenic-derived denudation rates

In the headwater of the Lanyang River, individual sub-basins associated to the Mimoden (Ilan-1), Madan (Ilan-2), and Jekejo (Ilan-3) rivers have been sampled (Figs. 4 and 5). The Jekejo watershed is characterized by an area of 28 km^2, has a Strahler Order of 5 and drains the Miocene Lushan formation towards the southeastern headwater area of the Lanyang watershed. Both Mimoden and Madan watersheds are characterized by an area of 9 km^2, and a Strahler Order of 4. The Mimoden watershed drains the Oligocene formations whereas the Madan basin drains both the Miocene and Oligocene formations (Table 2). For the three headwater sub-basins, the total channel lengths are on the order of 30 km (Mimoden and Madan) and 90 km (Jekejo). The observed differences in basin geometrical properties are mainly controlled by the lithology, the Miocene formation being composed of more argillite and slate than

Table 3
In situ-produced ^{10}Be measurements in river sand samples (localisation on Fig. 4).

Sample	Basin	Scaled surface production rate (at./g/yr)[a]			Quartz weight dissolved (g)	(^{10}Be/^{9}Be)				[^{10}Be] (at./g)		Denudation (mm/yr) (Granger et al., 1996)[f]		Denudation (mm/yr) (equation (5))[g]		Integration time (yr)	
		Neutrons	Negative muons	Fast muons		Measured ($\times10^{-15}$)	N[b]	Chi-square [c]	Max. value ($\times10^{-15}$)[d]	Value	Error[e]	Value	Error	Value	Error[h]	Value	Error
Tandetron																	
Ilan-1	Mimoden	13.00	0.20	0.09	18.27	9.79	8	4.39	N.A.	9212	4408	N.A.	N.A.	1.44	0.56	805	405
Ilan-4	Lanyang	14.04	0.22	0.09	15.27	11.50	11	6.41	N.A.	13264	5262	N.A.	N.A.	1.08	0.35	1074	457
Ilan-10	Lanyang	12.13	0.19	0.08	22.78	8.75	14	5.93	N.A.	6741	2780	N.A.	N.A.	1.83	0.62	632	278
Ilan-12	Lanyang	11.32	0.17	0.08	19.97	9.53	9	4.71	N.A.	8211	3794	N.A.	N.A.	1.36	0.53	824	402
Ilan-16	Dowan	9.20	0.14	0.06	14.40	6.32	4	1.65	9.49	13681	N.A.	0.53	N.A.	N.A.	N.A.	N.A.	N.A.
Ilan-22	Tiengou	7.89	0.12	0.05	10.17	5.33	5	1.53	7.71	15835	N.A.	0.39	N.A.	N.A.	N.A.	N.A.	N.A.
Ilan-3	Jekejo	15.50	0.24	0.10	9.54	4.42	4	0.94	6.63	14453	N.A.	0.84	N.A.	N.A.	N.A.	N.A.	N.A.
Process Blank						1.71	1	3.84									
Aster																	
Ilan-2	Madan	11.63	0.18	0.08	25.56	3.07	14	0.50	1.58	1284	N.A.	7.09	N.A.	N.A.	N.A.	N.A.	N.A.
Ilan-5	Fubuer	13.33	0.20	0.09	19.28	2.85	11	0.00	1.40	1502	N.A.	6.94	N.A.	N.A.	N.A.	N.A.	N.A.
Ilan-7a	Lanyang	12.48	0.19	0.08	27.27	3.90	8	0.51	2.98	2255	N.A.	4.33	N.A.	N.A.	N.A.	N.A.	N.A.
Ilan-8	Lanyang	12.47	0.19	0.08	17.77	4.87	17	2.44	3.75	4398	N.A.	2.22	N.A.	N.A.	N.A.	N.A.	N.A.
Ilan-23	Lanyang	10.44	0.16	0.07	19.09	2.69	12	0.03	1.16	1235	N.A.	6.61	N.A.	N.A.	N.A.	N.A.	N.A.
Ilan-9a	Lanyang	12.17	0.19	0.08	24.45	6.11	18	4.52	N.A.	4937	2324	N.A.	N.A.	2.56	0.96	461	228
Ilan-11b	Sechong	12.68	0.19	0.08	19.02	5.17	24	3.85	N.A.	5635	2876	N.A.	N.A.	2.34	0.94	505	269
Ilan-13	Lanyang	10.99	0.17	0.07	24.22	5.19	26	4.16	N.A.	4431	2174	N.A.	N.A.	2.58	1.00	458	236
Ilan-14	Lanyang	9.65	0.15	0.06	19.68	5.17	27	4.24	N.A.	5324	2589	N.A.	N.A.	1.88	0.72	627	320
Process blank						2.84	28	3.84									

N.A. not available.

[a] Production rates are calculated following Stone (2000) for altitudinal and latitudinal scaling and according to Dunne et al. (1999) for geomorphic shielding (see text).

[b] N refers to the number of counts during 3600 s of measurement.

[c] Chi-square test according to Ward and Wilson (1978).

[d] Maximum value of isotopic ratio is calculated as follow $R_{max} = (R_{mes} + dR_{mes}) - (R_{bk} - dR_{bk})$ where R_{mes}, R_{bk} are the measured and blank ratios. and dR_{mes} and dR_{bk} their associated uncertainties.

[e] Uncertainties on ^{10}Be concentrations are calculated using the standard error propagation method using the quadratic sum of the relative errors associated to the counting statistics, AMS internal error (5% for Tandetron, 0.5% for ASTER), and error associated to process blanks.

[f] Denudation rates are calculated using a homogeneous material with a density of 2.4 g/cm^3 and the equation in Granger et al. (1996).

[g] Denudation rates are calculated considering both neutrons and muons and equation (5).

[h] Uncertainties on denudation rates are calculated propagating the uncertainties associated to ^{10}Be concentrations as well as 6% error on production rates (Stone, 2000) and 14% error on the density (see text).

the Oligocene formations on the left-hand side of the Lanyang Valley. The in situ-produced ^{10}Be concentrations measured in the river sands sampled at the outlets of the three headwater basins reflect denudations rates that are 1.4 ± 0.6 mm/yr (Ilan-1), >7.1 mm/yr (Ilan-2), and >0.8 mm/yr (Ilan-3) (Table 3).

Along the course of the Lanyang River, individual sub-basins associated to the Fubuer (Ilan-5), Sechong (Ilan-11b), Dowan (Ilan-16) and Tiengou (Ilan-22) rivers have been sampled (Figs. 4 and 5). The Fubuer watershed is characterized by an area of 26 km^2, has a Strahler Order of 5 and drains the Oligocene formations of the Hsüehshan Range. The three other sub-basins drain the Miocene formation that constitutes the Backbone Range. They are characterized by areas of 30 km^2 (Sechong), 44 km^2 (Dowan), and 36 km^2 (Tiengouer), and by Strahler Orders of 5 (Table 2). The in situ-produced ^{10}Be concentrations measured in the river sands sampled at the outlets of these sub-basins yielded denudations rates that are >6.9 mm/yr (Ilan-5), 2.3 ± 0.9 mm/yr (Ilan-11b), >0.5 mm/yr (Ilan-16), and >0.4 mm/yr (Ilan-22) (Table 3).

In addition to the sampled sub-basins, a total of nine samples have been taken along the course of the main trunk (Table 2 and Fig. 4). They all correspond to the Lanyang watershed that drains both the Hsüehshan and the Backbone geological formations (Fig. 4), with areas ranging from 47 km^2 (Ilan-4) to 376 km^2 (Ilan-14) and Strahler Orders ranging from 5 (Ilan-4) to 7 (Ilan-14) (Table 2). The in situ-produced ^{10}Be concentrations measured in the river sands yielded cosmogenic-derived denudation rates that are ranging from 1.1 ± 0.4 mm/yr (Ilan-4) to >6.6 mm/yr (Ilan-23), but a majority (6) are comprised between 2 and 3 mm/yr (Table 3).

The pattern of spatial variation observed in the cosmogenic-derived denudation rates can be influenced by the distribution and proportion of landslides affecting the hillslopes (e.g., Niemi et al., 2005). To tackle this issue, we mapped the areas where the lack of vegetation cover indicates areas of rock mass-wasting (Fig. 4) and report the percentage of area affected by landslides versus the drainage basin areas when available (Table 2). In a general manner, the lack of vegetation cover can only be considered as a proxy for very recent landslides. However, it seems that the hillslopes of the Lanyang watershed are not dramatically affected by mass-wasting events. Nevertheless, it does not preclude that any significant landslides may have occurred in the area during the last millennium. Among the sampled sub-basins, the Mimoden watershed is the only one to be significantly affected by mass-wasting, 18.8% of its surface being unvegetated (Table 2). Since mass-wasting processes are expected to yield large quantities of rock and soils that have been shielded from cosmic rays, in situ-produced ^{10}Be concentrations are expected to be lower than what they should be, and thus cosmogenic-derived denudation rates to be overestimated. In the case of the Lanyang sub-basins, we do not see any evidence showing that the recent mass-wasting processes may have affected the spatial pattern of cosmogenic-derived denudation rates. To the contrary, the Mimoden basin, with the highest proportion of surface affected by recent landslides, is characterized by a cosmogenic-derived denudation rate which is among the lowest of our dataset (Table 3).

4.4. Integration time scale and background denudation rate

The integration time scale (T_{eff}) reflects the time during which denudation removes a rock depth equivalent to one absorption free path for cosmic ray particles (Lal, 1991). Under the conditions of steady-state equilibrium, the integration time scale and the denudation rate are related by the expression:

$$T_{eff} = \frac{\Lambda}{\rho \cdot \varepsilon} \quad (6)$$

The integration time scales have been calculated only for the samples providing reliable denudation rates (Table 3). Using a mean free path of 160 g/cm^2 for spallogenic particles and a density of 2.1 ± 0.3 g/cm^3 for the regolith layer, allows estimating integration time scales ranging from 461 ± 228 to 1074 ± 457 years (Table 3). In the calculation, the uncertainties associated with the denudation rates are directly propagated to estimate the uncertainties associated with the integration time scale values. Those integration times are long enough to consider that the measured cosmogenic nuclide concentrations should be relatively insensitive to recent change in denudation (such as human activity or typhoons). Among all the samples that have been analyzed for this study, only eight fulfill the necessary requirement to be significantly different from the process blanks. However, in spite of the differences in either geomorphological context (from one sub-basin to another) or in external transitory processes that may play an important role (e.g., landslides), the denudation values are remarkably constant ranging from 1.1 ± 0.4 to 2.6 ± 1.0 mm/yr (Table 3). To compare the denudation rates derived from cosmogenic measurements to those derived from modern suspended load measurements (see below), we will consider that a background value of 2 ± 1 mm/yr is representative for the Lanyang River watershed denudation rate. This value corresponds to the most downstream sample (Ilan-14), which is associated to the largest watershed and thus integrates all the processes described above.

5. Denudation rates derived from modern suspended load measurements

In order to compare the short-term time span with the cosmogenic time scale, an analysis of river sediment transport and erosion rates was done using the data from three stations, two of which are along the main course of the Lanyang River (H001 and H006) whereas the third one (H019) corresponds to a smaller watershed draining from the Hsüehshan Range (Fig. 1B). In Taiwan, the collection and storage of hydrological data has been controlled since 1936 by the Water Conservancy Agency (WCA) of the Central Government. The "Hydrological year book of Taiwan", published on a yearly basis, contains information on water discharge and suspended sediment records, with updated compilation at the WCA website (http://www.wra.gov.tw/). At each hydrological station, the discharge was measured daily and suspended sediment contents were measured on a monthly basis using depth-integrating suspended sediment tools. Because of this relatively low sampling frequency, reliable results cannot be obtained from the suspended sediment data considered alone. The daily records of discharge must be used, which requires preliminary quantification of relationships between discharge and sediment contents.

Fleming (1975) proposed a simple relationship between discharge and sediment content, using data from 250 different databases of drainage basins in the world. The corresponding equation is:

$$C = a \cdot Q_w^b \quad (7)$$

where C is the instantaneous suspended sediment concentration, C (in mg/l, often called p.p.m.), Q_w the water discharge (usually in c.m.s., *i.e.*, m^3/s). The empirical constants a and b are determined using the available couples of measurements of Q_w and C. Knowing C, the suspended load of a known station, the instantaneous suspended sediment discharge, Q_s (in metric tons/day), is obtained as:

$$Q_s = kCQ_w \quad (8)$$

where k is a conversion factor that depends on the adopted units (0.0864 with the above units). Using equations (7) and (8), one easily calculates the quantity of sediments as a function of water discharge:

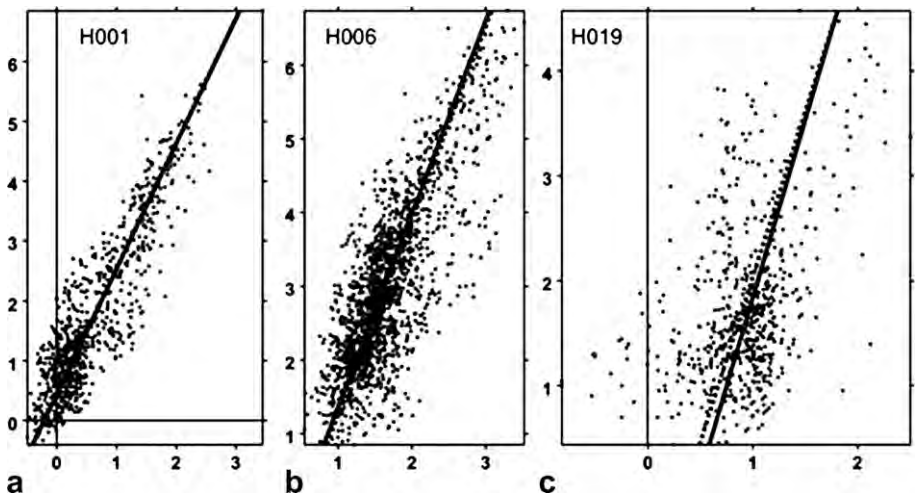

Fig. 6. Analysis of water discharge and sediment suspension at three hydrological stations of the Layang River Basin (a H001, b H006 and c H019). Location of stations is shown in Fig. 1. Abscissas: decimal logarithm of water discharge (m^3/s). Ordinates: decimal logarithm of sediment contents (metric ton/day). Linear regressions based on couples of data Q_w and Q_s collected from 1941 to 2005 (Water Conservancy Agency of Central Government of Taiwan). Results of numerical regression analyses are shown as dotted line for least square minimization and solid line for least distance minimization. Corresponding numerical parameters are listed in Table 4.

$$Q_S = AQ_W^B, \text{ with } A = ka \text{ and } B = b + 1. \quad (9)$$

Li et al. (2005) proposed the use of equation (9), rather than (7), because it allows clear separation between the quantities of water, Q_W and sediment, Q_S. In equation (8), Q_W is implicitly present on the left side because C is a function of both Q_S and Q_W. Li et al. (2005) consequently used a two-step process to evaluate the quantity of suspended sediment carried by rivers from the hydrological station data. First, the parameters A and B of the power law (9) are calculated, as shown in Fig. 6 and Table 4, from a simple linear regression using all available couples (usually about one per month) of decimal logarithms of Q_S and Q_W:

$$\log_{10}Q_S = \log_{10}A + B\log_{10}Q_W \quad (10)$$

Second, the same relationship is applied to the complete set of discharge data (usually one per day), resulting in the evaluation of the total quantity of suspended sediment, S, carried by the river at the corresponding hydrological station from day d_1 to day d_2 (e.g., one year):

$$S = A\sum_{d_1}^{d_2} Q_W^B \quad (11)$$

where Q_W and Q_S are expressed in m^3/s and metric tons/day, respectively.

As noted by Li et al. (2005), the common absence of sediment content measurement when discharge is low in Taiwan's rivers introduces a systematic bias towards high values of C and Q_S while considering the raw couples of data. The proposed extrapolation method allows avoiding this undesirable effect. Another bias was introduced by the presence in the printed data lists of repeated values that did not correspond to any actual measurement, which required careful examination and evaluation of these lists.

Two difficulties still remain, both leading to underestimate sediment transport, and hence erosion rates. First, according to unpublished data from several major rivers in Taiwan, twin-step laws of type (9) often deserve consideration, because abnormally high conditions of water discharge during typhoons result in flow regimes with significantly higher values of B. However, the analysis of the data from the Lanyang River did not reveal this effect so that a single relationship (9) could be used at each station (Fig. 6). Second, the coarser sand grains and pebbles rolling, sliding, and saltating on the riverbed are by definition ignored in suspended sediment load data, although this bed load contribution to sediment transport may be significant. At a typical station along the Kaoping River of Southern Taiwan, numerical modeling simulating scouring and deposition suggested that bed load may represent 12–42% of the total load (Lee and Hsieh, 2003).

As an example, at station H006, consideration of 1540 couples of simultaneously recorded values Q_W and Q_S allowed determination of values of 2.63 and −1.37 for A and B respectively, with a relatively low mean square root of distance from points to curve (0.09) indicating a good fit (Table 4). Then, the equation (11) applied to 20,454 daily discharge data Q_W yielded an average value of 56,500 tons of sediment per day. These values correspond to a sediment transport of about 2×10^7 metric tons per year for an average water discharge of 62.8 m^3/s (the minimum and maximum recorded values of discharge being 7.6 m^3/s on Feb. 13th, 1996 and 637 m^3/s, on Aug. 19th, 1984). This average Q_S implies a minimum erosion rate of about 2.5 g/cm^2 yr (25,000 metric tons/km^2 per year) for a basin

Table 4
Numerical results of the analysis of water discharge and sediment suspension at three hydrological stations of the Layang River Basin (H001, H006 and H019). Location of stations in Fig. 1, regression analysis diagrams in Fig 6.

Station	H001	H006	H019
N	765	1540	604
A	2.09	2.63	3.15
B	0.46	−1.37	−1.11
$Q_S = 10^B Q_W^A$	$Q_S = 2.884Q_W^{2.09}$	$Q_S = 0.043Q_W^{2.63}$	$Q_S = 0.078Q_W^{3.15}$
msrd	0.076	0.087	0.139
A'	2.09	2.62	3.38
B'	0.48	−1.28	−1.54
$Q_S = 10^{B'} Q_W^{A'}$	$Q_S = 3.020Q_W^{2.09}$	$Q_S = 0.052Q_W^{2.62}$	$Q_S = 0.029Q_W^{3.38}$
md	0.215	0.222	0.281

N: number of couples of data Q_W and Q_S collected from 1941 to 2005 (Water Conservancy Agency of Central Government). Results of least square adjustment (the sum of squares of the distances between data point and straight line is made minimum): A and B, parameters of equation $y = Ay+B$; where x and y are the decimal logarithms of Q_W and Q_S respectively. Results of least value adjustment (the sum of distances between data point and straight line is made minimum): A' and B', same definition as for A and B. The resulting laws giving Q_S as a function of Q_W are indicated in both cases, and the average residuals are given as mean square root of distance (*msrd*) for the least square adjustment and mean distance (*md*) for the least value adjustment. Explanations and units given in the text.

Table 5
Numerical results of the determination of suspended sediment transport at three hydrological stations of the Layang River Basin (H001, H006 and H019; Fig. 1).

Station	H001	H006	H019
ND	10.657	20.454	8.401
W	41.8	62.8	10.5
BA	446.7	820.7	101.4
S/ND	12.993	53.121	2.593
S′/ND	13.606	59.880	2.837
DR	10.622	23.616	9.344
DR′	11.132	26.645	10.220
dr	0.44	0.98	0.39
dr′	0.46	1.11	0.43

ND, number of days with discharge data Q_w collected until the end of 2006. Measurements started in 1948, 1950, 1974 and 1984 for stations H001, H006, H017 and H019 respectively, but interruptions occurred and published lists are wrong for year 2001 (data from Water Conservancy Agency of Central Government).
W, average discharge Q_w in m^3/s.
BA, drainage basin area for each station, in km^2.
S/ND, resulting average quantity of suspended sediment Q_s in metric tons/day, calculated from equation (5).
S′/ND, same calculations with parameters A′ and B′ instead of A and B (see Table 4 and Fig 6 for parameter determination).
DR and DR', resulting denudation rates in metric tons/km^2 yr.
dr and dr', corresponding denudation rates in cm/yr. assuming an average sediment density of 2.4 g/cm^3.

area of 821 km^2. This value is of the same order of magnitude as, but significantly higher than, the value of 730 mg/cm^2 yr indicated by Lee (1976) at the same downstream location of the Lanyang River. Assuming an average density of 2.4 g/cm^3 for dry transported sediment, the erosion rate derived from suspended load data for the entire Lanyang drainage basin averages 10 mm/yr.

Three major hydro-stations of the Lanyang River basin have thus been analyzed (Fig. 6 and Table 4). In the first approximation, for couples of values Q_S and Q_W the data points fit a straight line in logarithmic co-ordinates, consistent with a power law of type (9). Whether or not the regression involves least square minimization or simple minimization of the distances from data points to the straight line do not significantly modify the result. The resulting values of A fall in the range 2–4 and the values of B fall in the range −1.5–0.5.

It is interesting to compare these results obtained at station H006 in the downstream course of the Lanyang River with the results of the other two stations (Table 5). The station H001 is located upstream with respect to H006, near the junction between the steepest, mountainous course of the Lanyang River and the Ilan Plain. The amount of suspended sediment transported is 13,300 metric tons/day, which is 24% of that obtained at station H006. The calculated denudation rate, about 11,000 metric tons/km^2 per year, represent 44% of that obtained from station H006, for a drainage basin that covers an area 54% of that of station H006. The comparison between these percentages indicates that a large proportion of suspended sediment brought to the sea comes from tributaries located downstream of station H001. Another comparison can be done between the Lanyang River Basin and the independent Ilan River Basin where station H019 reveals denudation rates similar to those of H001 despite much smaller discharge and a smaller size of the upstream drainage basin. Considering the drainage pattern distribution (Fig. 1), these two comparisons suggest that similar short-term erosion rates of about 4–5 mm/yr on average prevail around the higher Lanyang Valley on both sides of the Lishan Fault and in the Ilan River basin on the eastern flank of the Hsüehshan Range (compare H001 and H019 in Table 5), whereas higher rates prevail in the portion of the Lanyang River drainage basin closer to the Ilan Plain, where several tributaries come from the mountains on both sides, with the Lushan Formation south of the Ilan Plain and the rivers of the Hsüehshan Range to the northwest.

6. Discussion and conclusion

Denudation rate refers to the total rate of material removal near the Earth's surface. It is the combination of physical (erosion) and chemical (weathering) processes. Cosmogenic nuclides accumulate as material moves towards the surface by the removal of material above, and thus always reflect the combination of both processes. In Taiwan, the suspended load and bed load components are largely dominant compared to the dissolved fraction (Lee, 1976; Li et al., 2005). The simplification to call the cosmogenic nuclide-derived denudation rates "erosion rates" can be done, which makes the comparison with those derived from river load gauging easier.

In the upper-Lanyang watershed, the denudation rate derived from in situ-produced ^{10}Be concentrations averages 2 ± 1 mm/yr (over the last several hundreds of years). In the same watershed, the erosion rate given by the hydrological station H001 is 4.6 mm/yr (over the last 50 years), which is thus 2–5 times higher. If one assumes that the cosmogenic-derived denudation rate is representative for the entire Lanyang Watershed, then comparison with the hydrological station H006 makes the discrepancy even greater. In addition, it has to be underlined that the bed load is not considered for the calculation of erosion rates from river load gauging. Referring to the numerical modeling by Lee and Hsieh (2003), the total modern erosion rate in the upstream part of the Lanyang Watershed might well fall in the range 5–7 mm/yr.

In other geological and climatic contexts, cosmogenic-derived denudation rates have already been compared to river load gauging-derived erosion rates (Ivy-Ochs and Schaller, 2009). When the cosmogenic and river load-derived rates are in agreement, the authors suggested that the landscape might be in equilibrium (Clapp et al., 2001; Matmon et al., 2003; Vance et al., 2003). When the cosmogenic-derived rates were higher than those derived from river load gauging, the discrepancy was attributed to either stochastic erosional events or bias in the river gauging data collection (Kirchner et al., 2001; Schaller et al., 2001). In the case of the Lanyang Watershed, the cosmogenic-derived rates are lower than those derived from river load gauging. Since hydrological data spanned time scales that are on the order of several tens of years, they are more sensitive to recent change in erosion rates in relation with human activity or extreme erosional events (e.g., earthquakes and typhoons). In that case, the cosmogenic-derived denudation rates should be closer to the natural background denudation value (Brown et al., 1995, 1998; Hewawasam et al., 2003). However, it is worth noting that the portion of the Lanyang Watershed where cosmogenic measurements have been done is relatively free of human activity compared to the Ilan plain downstream, and the 2-fold difference in erosion rates between stations H006 and H001 might well reflects this difference. If it is so, the discrepancy with the cosmogenic-derived denudation rate is then most probably due to the effects of stochastic erosional events on the short-time scale rather than to recent change due to human activity.

In the same region of North-eastern Taiwan (Nahutashan area), Siame et al. (2007) estimated maximum denudation rates from bedrock exposure located above the maximum Equilibrium Line Altitude (e.g., Hebenstreit et al., 2006). One sampling site was located along the crest of the eastern ridge bordering the Southeast valley (Fig. 1; NHTS11), and corresponded to a quartz vein embedded within schist rocks. Another sampling site was located close to the summit of Nanhutashan Main Peak (Fig. 1, NHTS23), and corresponded to a weathered quartzite strata also intercalated within schist rock strata. Since these bedrock exposures are supposed to have not been overridden by glaciers during the Last

Glacial episode, their exposure duration may be long enough to ensure that steady-state concentrations were reached. Under this assumption, the measured ^{10}Be concentrations allowed estimating maximum denudation rates of 0.10 ± 0.02 mm/yr. Though limited in space, these two samples suggest that the denudation rate affecting rock on crest and summits might be 10 times lower than the cosmogenic-derived estimated within the Lanyang river belt.

On one hand, thermo-mechanical and kinematic models suggest long-term rates of denudation ranging between 2 and 3 mm yr^{-1} throughout the Taiwan belt (Fuller et al., 2006; Simoes et al., 2007). The cosmogenic-derived denudation rates determined in the Lanyang Watershed are thus close to this long-term estimate whereas the erosion rates from river suspended loads are significantly higher. This underlines the fact that, in such dynamic environment as Taiwan, suspended load data might not yield erosion rates that are representative for those prevailing at geological time scales. Integrated over several hundreds of years, the cosmogenic-derived denudation rates are less sensitive to the extreme erosional events, and thus more representative. On the other hand, it seems that denudation rates on ridge crests and summits might be one order of magnitude lower than those determined from low thermochronological data and in situ-produced ^{10}Be in river-borne sands. This discrepancy questions the steady-state equilibrium of Taiwan's topography, and is worth to be examined at the scale of the whole Taiwan belt through a study including more basin-wide and summit data.

Acknowledgements

Meanwhile this paper was written and submitted, Jacques Angelier passed away. Lionel Siame would like to dedicate this article to his memory. We are gratefull for the constructive comments provided by two anonymous reviewers. This research is part of the scientific cooperation between France and Taiwan within the framework of agreements between National Science Council, Institut Français à Taiwan, and Centre National de la Recherche Scientifique, including the International Laboratory (LIA-536 CNRS/NSC) "ADEPT" (Active Deformation and Environment Project for Taiwan). Funding for travel and fieldwork were provided by the PICS-Taiwan and Central Geological Survey (CGS) of Taiwan. We would like to thank Shao Ping-Hua, You Su-Lin and Chi Xiao-Mei from CGS for their help on the field, as well as Rémi Gamerre and Louise Watremez for their work at the laboratory. The French AMS national facility ASTER (CEREGE, Aix-en-Provence) is supported by the INSU/CNRS, the French Ministry of Research and Higher Education, IRD and CEA. We are grateful to Maurice Arnold, Georges Aumaître and Karim Keddadouche for their invaluable help during the ^{10}Be AMS measurements.

Annex 1: Schmidt Hammer rebound measurements.

Sample	LON	LAT	ELE	Val1	Val2	Val3	Val4	Val5	Val6	Val7	Val8	Val9	Val10	Average (kg/cm^2)		Geologica formation	Lithology
	TWD67 WGS84 (m)			(kg/cm^2)										Value	Error		
1	298,273	2,723,299	1015	337	370	287	256	304	256	322	241	420	386	318	60	Os	Slate
2	298,521	2,723,139	977	256	256	211	287	322	353	322	226	304	241	278	47	Os	Slate
3	298,434	2,723,033	946	370	402	472	489	437	472	489	489	370	420	441	48	Os	Sandy-Slate
4	298,588	2,722,917	888	563	420	582	642	526	563	622	544	582	544	559	60	Os	Sandy-Slate
5	299,109	2,722,510	685	241	287	322	337	256	353	322	226	241	287	287	45	Os	Slate
6	299,985	2,722,459	542	211	287	322	172	304	304	322	287	226	287	272	51	Os	Slate
7	300,828	2,722,139	441	526	489	489	544	544	472	526	601	563	544	530	39	Os	Sandy-Slate
8	301,132	2,721,497	356	386	256	226	172	197	304	322	197	287	322	267	69	M1	Slate
9	300,356	2,720,507	345	322	353	322	256	256	353	353	287	211	287	300	49	M1	Slate
10	303,144	2,710,564	1888	304	272	337	241	420	455	437	437	420	455	378	81	M1	Slate
11	302,347	2,711,580	1884	304	241	337	256	172	287	304	322	337	287	285	51	M1	slate
12	302,437	2,714,706	1052	489	437	420	455	322	353	386	455	489	402	421	56	M1	Sandy-Slate
13	300,425	2,716,865	631	304	322	337	304	226	322	386	226	370	322	312	52	M1	slate
14	299,650	2,718,585	443	104	84	65	104	74	148	160	104	104	104	105	30	M1	Weathered slare
15	300,338	2,720,503	372	544	353	489	455	437	386	437	455	455	420	443	52	M1	Sandy-Slate
16	288,090	2,704,532	1039	160	172	148	241	287	322	304	287	226	322	247	68	M1	Slate
17	286,032	2,701,137	1432	664	794	817	772	563	728	794	728	910	489	726	125	EO2	Sandstone
18	286,032	2,701,137	1432	272	211	272	322	337	241	226	370	322	226	280	55	EO2	Slate
19	285,837	2,700,985	1452	563	817	472	455	563	563	601	489	420	563	551	111	EO2	Sandstone
20	285,516	2,700,451	1504	684	772	1006	772	684	772	817	910	684	817	792	104	Os	Sandstone
21	285,565	2,700,306	1536	910	910	1106	817	910	772	772	63	960	910	813	281	Os	Sandstone
22	286,523	2,699,670	1750	226	256	287	322	197	304	353	370	287	304	291	53	M1	Slate
23	286,423	2,700,025	1643	256	256	226	241	172	197	226	197	172	322	227	46	M1	Slate
24	285,626	2,700,287	1549	455	544	684	642	772	601	863	817	794	772	694	132	Os	Sandy-Slate
25	287,672	2,704,446	1127	526	526	472	544	544	507	601	544	563	563	539	35	EO2	Sandy-Slate
26	288,078	2,704,867	1219	256	322	322	386	322	241	353	337	287	353	318	45	EO2	Slate
27	288,084	2,705,024	1289	287	304	353	322	287	353	353	337	287	304	319	29	EO2	Slate
28	288,084	2,705,024	1289	622	582	507	489	507	642	489	544	601	507	549	58	EO2	Sandy-Slate
29	287,930	2,705,287	1346	981	1006	910	1030	910	960	750	863	960	817	919	88	EO2	Sandstone
30	288,647	2,705,059	1006	601	706	622	622	750	684	706	706	684	750	683	52	M1	Sandy-Slate
31	288,669	2,705,152	1002	353	420	489	386	353	402	489	322	370	437	402	57	M1	Slate
32	288,876	2,705,532	974	817	684	706	772	750	794	684	772	728	886	759	63	M1	Sandy-Slate
33	288,887	2,707,442	1094	582	601	772	840	684	684	863	728	684	840	728	99	EO2	Sandstone
34	289,232	2,707,432	1053	489	489	563	601	544	642	622	563	622	544	568	54	EO2	Sandstone
35	290,933	2,707,128	837	601	563	489	563	642	526	582	563	582	544	566	42	M1	Sandstone
36	291,791	2,708,183	790	337	370	386	402	353	489	386	420	337	420	390	46	M1	Slate
37	292,161	2,709,065	733	886	817	863	886	794	863	817	817	910	863	852	38	M1	Sandstone

(*continued*)

Sample	LON	LAT	ELE	Val1	Val2	Val3	Val4	Val5	Val6	Val7	Val8	Val9	Val10	Average (kg/cm^2)		Geologica formation	Lithology
	TWD67 WGS84 (m)			(kg/cm^2)										Value	Error		
38	292,161	2,709,065	733	322	337	304	272	256	287	304	256	322	256	292	31	M1	Slate
39	292,457	2,709,538	779	226	226	211	256	197	272	256	241	226	211	232	24	M1	Slate
40	293,486	2,711,813	681	226	226	197	172	287	256	353	322	322	353	271	65	M1	Slate
41	294,859	2,713,849	621	304	272	304	337	256	370	287	304	272	322	303	34	M1	Slate
42	295,616	2,715,985	557	226	241	226	256	241	226	256	256	197	226	235	19	M1	Slate
43	297,297	2,717,540	481	563	642	489	489	526	642	706	684	642	728	611	88	M1	Sandstone
44	297,297	2,717,540	481	489	526	420	526	507	563	489	622	526	563	523	54	M1	Sandy-Slate
45	297,297	2,717,540	481	172	197	226	226	172	226	197	185	172	197	197	22	M1	Slate
46	297,150	2,717,957	489	563	684	526	664	642	526	642	642	642	642	617	57	M1	Sandy-Slate

To illustrate the measurement data and their associated uncertainties, we used the sum of the Gaussian probability distributions (e.g., Deino and Potts, 1992), already used by different authors for dating purposes (*i.e.*, Daëron et al., 2004; Lowell, 1995; Taylor, 1997). In the case of Schmidt hammer measurements, the Gaussian probability distributions for the rebound values are determined using:

$$P_{sum}(Rv) = \sum_i e^{-\frac{(Rv-Rv_i)^2}{2\rho_i^2}} / \rho_i\sqrt{2\Pi}$$

where Rv is the rebound value, Rv_i is the rebound value for site i and σ_i is the associated standard deviation (Table 1). A probability value less than 0.05 indicates that there is a significant amount of non-analytical error in the dataset, and that one or more samples are outliers. In such a case, cumulative frequency plots are generally bimodal in shape, with the secondary peak identifying outliers.

Editorial handling by: R. Grun

References

Arnold, M., Merchel, S., Bourlès, D.L., Braucher, R., Benedetti, L., Finkel, R.C., Aumaître, G., Gottdang, A., Klein, M., 2010. The French accelerator mass spectrometry facility ASTER: improved performance and developments. Nuclear Instruments and Methods in Physics Research Section B 268, 1954–1959. doi:10.1016/j.nimb.2010.02.107.

Aydin, A., Basu, A., 2005. The Schmidt hammer in rock material characterization. Engineering Geology 81, 1–14.

Beaumont, C., Fullsack, P., Hamilton, J., 1992. Erosional control of active compressional orogens. In: McClay, K.R. (Ed.), Thrust Tectonics. Chapman & Hall, London, England, pp. 1–18.

Beaumont, C., Kooi, H., Willett, S.D., 2000. Coupled tectonic-surface process models with applications to rifted margins and collisional orogens. In: Summerfield, M.A. (Ed.), Geomorphology and Global Tectonics. Wiley, pp. 29–55.

Bierman, P.R., Nichols, K.K., 2004. Rock to sediment-slope to sea with Be-10-rates of landscape change. Annual Review of Earth and Planetary Sciences 32, 215–255.

Braucher, R., Bourlès, D.L., Brown, E.T., Colin, F., 2003. Reevaluation of ^{10}Be production by muons. Earth and Planetary Science Letters 211 (3–4), 251–258.

Brown, E.T., Stallard, R.F., et al., 1995. Denudation rates determined from the accumulation of in situ-produced ^{10}Be in Luquillo experimental forest, Puerto Rico. Earth and Planetary Science Letters 129, 193–202.

Brown, E.T., Stallard, R.F., et al., 1998. Determination of predevelopment denudation rates of an agricultural watershed (Cayaguas River, Puerto Rico) using in-situ-produced ^{10}Be in river-borne quartz. Earth and Planetary Science Letters 160, 723–728.

Burbank, D.W., 2002. Rates of erosion and their implications for exhumation. Mineralogical Magazine 66, 25–52.

Chen, C.-H., Ho, H.-C., Shea, K.-S., Lo, W., Lin, W.-H., Chang, H.-C., Huang, C.-H., Lin, C.-W., Chen, G.-H., Yang, C.-N., Lee, Y.-H., 2000. Geologic Map of Taiwan (1/500000). Central Geological Survey, Ministry of Economic Affairs, Taipei, Taiwan.

Chen, R.-F., Chan, Y.-C., Angelier, J., Hu, J.-C., Huang, C., Chang, K.-J., Shih, T.-Y., 2005. Large earthquake-triggered landslides and mountain belt erosion: the Tsaoling case, Taiwan. C.R. Geosciences 337, 1164–1172.

Chmeleff, J., von Blanckenburg, F., Kossert, K., Jakob, D., 2009. Determination of the ^{10}Be half-life by multi-collector ICP mass spectrometry and liquid scintillation counting. Goldschmidt Conference, Geochimica Cosmochimica Acta 73 (Suppl. 1), A221.

Clapp, E.M., Bierman, P.R., Nichols, K.K., Pavitch, M., Caffee, M., 2001. Rates of sediment supply to arroyos from upland erosion determined using in situ produced cosmogenic Be-10 and Al-26. Quaternary Research 55, 235–245.

Craig, K., Baker, B., Patton, P., 1988. Flood Geomorphology. Wiley-Interscience.

Dadson, S.J., Hovius, N., Chen, H., Dade, B., Hsieh, M.L., Willett, S.D., Hu, J.C., Horng, M.J., Chen, M.C., Stark, C.P., Lague, D., Lin, J.C., 2003. Links between erosion, runoff variability and seismicity in the Taiwan orogen. Nature 426, 648–651.

Daëron, M., Benedetti, L., Tapponnier, P., Sursock, A., Finkel, R.C., 2004. Constraints on the post ~25-ka slip rate of the Yammoûneh fault (Lebanon) using in situ cosmogenic ^{36}Cl dating of offset limestone-clast fans. Earth and Planetary Science Letters 227, 105–119.

Deino, A., Potts, R., 1992. Age-probability spectra from examination of single-crystal ^{40}Ar/^{39}Ar dating results: examples from Olorgesailie, Southern Kenya Rift. Quaternary International 13–14, 47–53.

Dunne, J., Elmore, D., Muzikar, P., 1999. Scaling factors for the rates of production of cosmogenic nuclides for geometric shielding and attenuation at depth on sloped surfaces. Geomorphology 27, 3–11.

Fleming, G., 1975. Computer Simulation Techniques in Hydrology. Elsevier, Amsterdam.

Fuller, C.W., Willet, S.D., Fisher, F., Lu, C.-Y., 2006. A thermomechanical wedge model of Taïwan cosntrained by fission-track thermochronology. Tectonophysics 425, 1–24.

Fuller, C.W., Willet, S.D., Hovius, N., Slingerland, R., 2003. Erosion rates for Taiwan mountain basin: new determinations from suspended sediment records and a stochastic model of their temporal variation. Journal of Geology 111, 71–87.

Gosse, J.C., Phillips, F.M., 2001. Terrestrial in situ cosmogenic nuclides: theory and application. Quaternary Science Reviews 20, 1475–1560.

Granger, D.E., Kichner, J.W., Finkel, R., 1996. Spatially-averaged long-term erosion rates measured from in situ-produced cosmogenic nuclides in alluvial sediment. Journal of Geology 104, 249–257.

Hartshorn, K., Hovius, N., Dade, W.B., Slingerland, R.L., 2002. Climate-driven bedrock incision in an active mountain belt. Science 297, 2036–2038.

Hebenstreit, R., Böse, M., Murray, A., 2006. Late pleistocene and early holocene glaciations in Taiwanese mountains. Quaternary International 147 (1), 70–75.

Hewawasam, T.F., von Blanckenburg, F., Schaller, M., Kubick, P.W., 2003. Increase of human over natural erosion rates in tropical highlands constrained by cosmogenic nuclides. Geology 3, 597–600.

Ho, C.-S., 1986. A synthesis of the geologic evolution of Taiwan. Tectonophysics 125, 1–16.

Horton, R.E., 1932. Drainage basin characteristics. Transactions of the American Geophysical Union 13, 350–370.

Horton, R.E., 1945. Erosional development of streams and their drainage basins: hydrophysical approach to quantitative morphology. Bulletin of the Geological Society of America 56, 275–370.

Hovius, N., Stark, C.P., Chu, H.-T., Lin, J.-C., 2000. Supply and removal of sediment in a landslide-dominated mountain belt: Central Range, Taiwan. Journal of Geology 108, 73–89.

Ivy-Ochs, S., Schaller, M., 2009. Examining processes and rates of landscape change with cosmogenic nuclides. In: Radioactivity in the Environment, vol. 16, pp. 231–294. Elsevier. doi:10.1016/S1569-4860(09)01606-4.

Kirchner, J.W., Finkel, R.C., Riebe, C.S., Granger, D.E., Clayton, J.L., King, J.G., Megahan, W.F., 2001. Mountain erosion over 10 yr, 10 k.y., and 10 m.y. time scales. Geology 29, 591–594.

Koons, P.O., 1989. The topographic evolution of collisional mountain belts: a numerical look at the southern Alps, New Zealand. American Journal of Science 289, 1041–1069.

Korschinek, G., Bergmaier, A., Dillmann, I., Faestermann, T., Gerstmann, U., Knie, K., von Gostomski, C., Maiti, M., Poutivtsev, M., Remmert, A., Rugel, G., Wallner, A., 2009. Determination of the ^{10}Be half-life by HI-ERD and liquid scintillation counting. Goldschmidt Conference, Geochimica Cosmochimica Acta 73 (Suppl. 1), A685.

Lal, D., 1991. Cosmic ray labeling of erosion surfaces: in-situ nuclide production rates and erosion models. Earth and Planetary Science Letters 104, 424–439.

Lavé, J., Avouac, J.-P., 2001. Fluvial incision and tectonic uplift across the Himalayas of central Nepal. Journal of Geophysical Research 106, 26561–26591.
Lee, H.-Y., Hsieh, H.-M., 2003. Numerical simulations of scour and deposition in a channel network. International Journal of Sediment Research 18 (1), 1–17.
Lee, J.-C., Angelier, J., Chu, H.-T., 1997. Polyphase history and kinematics of a complex major fault zone of the Taiwan mountain belt: the Lishan Fault. Tectonophysics 274, 97–115.
Lee, Y.-H., 1976. Denudation of Taiwan island since the Pleistocene epoch. Geology 4 (2), 105–107.
Li, F.-C., Angelier, J., Chen, R.-F., Hsieh, H.-M., Deffontaines, B., Luo, C.-R., Wu, T.-T., Lin, M.-C., 2005. Estimates of present-day erosion based on sediment transport in rivers: a case study in Taiwan. C.R. Geosciences 337 (13), 1131–1139.
Liu, C., Liu, J.-P., Milliman, J.D., Lin, S., 2006. Tectonic–Climatic Controls on Lanyang River (Taiwan) Discharge to the Southwestern Okinawa Trough. Ocean Sciences AGU Meeting, 20–24 February 2006, Honolulu, Hawaii.
Liu, T.-K., 1982. Tectonic implications of fission track ages from the Central Range, Taiwan. Proceedings of the Geological Society of China 25, 22–37.
Liu, T.-K., Chen, Y.-G., Chen, W.-S., Jiang, S.-H., 2000. Rates of cooling and denudation of the early Penglai orogeny, Taiwan, as assessed by fission track constraints. Tectonophysics 320, 69–82.
Liu, T.-K., Hsieh, S., Chen, Y.-G., Chen, W.-S., 2001. Thermo-kinematic evolution of the Taiwan oblique collision mountain belt as revealed by Zircon fission track dating. Earth and Planetary Science Letters 186, 45–56.
Lowell, T.V., 1995. The application of radiocarbon age estimates to the dating of glacial sequences: an example from the Miami sublobe, Ohio, USA. Quaternary Science Reviews 14, 85–99.
Matmon, A., Bierman, P.R., Larsen, M.C., Southworth, S., Pavitch, M., Caffee, M., 2003. Temporally and spatially uniform rates of erosion in the southern Appalachian Great Smoky Mountains. Geology 31, 155–158.
Merchel, S., Arnold, M., Aumaître, G., Benedetti, L., Bourlès, D.L., Braucher, R., Alfimov, V., Freeman, S.P.H.T., Steier, P., Wallner, A., 2008. Towards more precise ^{10}Be and ^{36}Cl data from measurements at the 10–14 level: influence of sample preparation. Nuclear Instruments and Methods in Physics Research Section B: Beam Interactions with Materials and Atoms 266 (22), 4921–4926.
Molnar, P., 2003. Nature, nurture and landscape. Nature 426, 612–614.
Molnar, P., England, P., 1990. Late Cenozoic uplift of mountain ranges and global climatic change: chicken or egg? Nature 346, 29–34.
Montgomery, D.R., Brandon, M.T., 2002. Topographic controls on erosion rates in tectonically active mountain ranges. Earth and Planetary Science Letters 201, 481–489.
Niemi, N.A., Oskin, M., Burbank, D.W., Heimsath, A.M., Gabet, E.J., 2005. Effects of bedrock landslides on cosmogenically determined erosion rates. Earth and Planetary Science Letters 237, 480–498.
Nishiizumi, K., Imamura, M., Caffee, M.W., Southon, J.R., Finkel, R.C., McAninch, J., 2007. Absolute calibration of ^{10}Be AMS standards. Nuclear Instruments and Methods in Physics Research Section B: Beam Interactions with Materials and Atoms 258 (2), 403–413.
Peckham, S.D., 1995. New results for self-similar trees with applications to river networks. Water Resources Research 31 (4), 1023–1029.
Raisbeck, G.M., Yiou, F., Bourlès, D., Lestringuez, J., Deboffle, D., 1987. Measurements of ^{10}Be and ^{26}Al with a tandetron AMS facility. Nuclear Instruments and Methods in Physics Research Section B: Beam Interactions with Materials and Atoms 29 (1–2), 22–26.
Raisbeck, G.M., Yiou, F., Bourlès, D., Brown, E., Deboffle, D., Jouhanneau, P., Lestringuez, J., Zhou, Z.Q., 1994. The AMS facility at Gif-sur-Yvette: progress, perturbations and projects. Nuclear Instruments and Methods in Physics Research Section B: Beam Interactions with Materials and Atoms 92 (1–4), 43–46.
Riebe, C.S., Kirchner, J.W., Finkel, R.C., 2004. Sharp decrease in long-term chemical weathering rates along an altitudinal transect. Earth and Planetary Science Letters 218, 421–434.
Ritter, D.F., Kochel, R.C., Miller, J.R., 1995. Process Geomorphology, third ed. W.C. Brown Publishers, Dubuque, Iowa.
Schaller, M., von Blanckenburg, F., Hovius, N., Kubik, P.W., 2001. Large-scale erosion rates from in situ produced cosmogenic nuclides in European river sediments. Earth and Planetary Science Letters 188, 441–458.
Siame, L.L., Chu, H.-T., Carcaillet, J., Lu, W.-C., Bourlès, D.L., Braucher, R., Angelier, J., Dussouliez, P., 2007. Glacial retreat history of Nanhuta Shan (North-east Taiwan) from preserved glacial features: the Cosmic ray exposure perspective. Quaternary Science Reviews 26, 2185–2200.
Simoes, M., Avouac, J.P., Beyssac, O., Goffé, B., Farley, K.A., Chen, Y.-G., 2007. Mountain building in Taiwan: a thermokinematic model. Journal of Geophysical Research 112, B11405.
Simpson, G., Schlunegger, F., 2003. Topographic evolution and morphology of surfaces evolving in response to coupled fluvial and hillslope sediment transport. Journal of Geophysical Research 108, 2300.
Small, E.E., Anderson, R.S., Repka, J.L., Finkel, R., 1997. Erosion rates of Alpine bedrock summit surfaces deduced from in situ ^{10}Be and ^{26}Al. Earth and Planetary Sciences Letters 150, 413–425.
Stone, J.O., 2000. Air pressure corrections for exposure dating. Journal of Geophysical Research 105, 23753–23759.
Strahler, A.N., 1952. Hypsometric (area-altitude) analysis of erosional topography. Geological Society of America Bulletin 63, 1117–1142.
Strahler, A.N., 1957. Quantitative analysis of watershed geomorphology. Transactions of the American Geophysical Union 8 (6), 913–920.
Strahler, A.N., 1958. Dimensional analysis applied to fluvially eroded landforms. Geological Society of America Bulletin 69, 279–299.
Strahler, A.N., 1964. Quantitative geomorphology of basins and channel networks. In: Chow, V.T. (Ed.), Handbook of Applied Hydrology. Mcgraw Hill Book Company, New York, pp. 4-39–4-76.
Summerfield, M.A., 1991. Global Geomorphology. Prentice Hall, Upper Saddle River, New Jersey.
Taylor, J.R., 1997. An Introduction to Error Analysis, the Study of Uncertainties in Physical Measurements, second ed. University Science Books, Sausalito, California.
Tucker, G.E., Bras, R.L.A., 2000. A Stochastic approach to modeling the role of rainfall variability in drainage basin evolution. Water Resources Research 36, 1953–1964.
Vance, D., Bickle, M., Ivy-Ochs, S., Kubik, P.W., 2003. Erosion and exhumation in the Himalaya from cosmogenic isotope inventories of river sediments. Earth and Planetary Science Letters 206, 273–288.
von Blanckenburg, F., 2005. The control mechanisms of erosion and weathering at basin scale from cosmogenic nuclides in river sediment. Earth and Planetary Science Letters 237, 462–479.
von Blanckenburg, F., Hewawasam, T., Kubik, P.W., 2004. Cosmogenic nuclide evidence for low weathering and denudation in the wet, tropical highlands of Sri Lanka. Journal of Geophysical Research 109, 1–22.
Ward, G.K., Wilson, S.R., 1978. Procedures for comparing and combining radiocarbon age determination: a critique. Archaeometry 20 (1), 19–31.
Whipple, K.X., Meade, B.J., 2004. Controls on the strength of coupling among climate, erosion, and deformation in two-sided, frictional orogenic wedges at steady state. Journal of Geophysical Research 109 (F1), F01011.
Whipple, K.X., Kirby, E., Brocklehurst, S.H., 1999. Geomorphic limits to climate-induced increases in topographic relief. Nature 401, 39–43.
Willett, S.D., 1999. Orogeny and orography: the effects of erosion on the structure of mountain belts. Journal of Geophysical Research 104, 28957–28981.
Willett, S.D., Fischer, D., Fuller, C., Yeh, E.-C., Lu, C.-Y., 2003. Erosion rates and orogenic-wedge kinematics in Taiwan inferred from fission-track thermochronometry. Geology 31, 945–948.
Willett, S.D., Slingerland, R., Hovius, N., 2001. Uplift, shortening, and steady state topography mountain belts. American Journal of Science 301, 455–485.